LA-UR-22-21415
Accepted Manuscript

Polybenzimidazole-derived carbon molecular sieve hollow fiber membranes with tailored oxygen selective transport

Seong, JongGeun
Lewis, Jeremy Charles
Thakkar, Harshul Vipul
Matteson, John Anthony
Berchtold, Kathryn A.
Martinez, Ulises
Benavidez, Angelica D.
Singh, Rajinder Pal

Provided by the author(s) and the Los Alamos National Laboratory (2022-02-22).

To be published in: Carbon

DOI to publisher's version: 10.1016/j.carbon.2022.02.033

Permalink to record:
http://permalink.lanl.gov/object/view?what=info:lanl-repo/lareport/LA-UR-22-21415

Journal Pre-proof

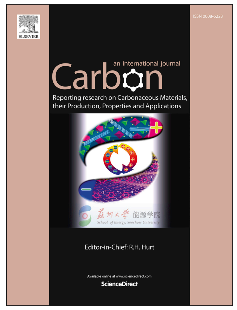

Polybenzimidazole-derived carbon molecular sieve hollow fiber membranes with tailored oxygen selective transport

Jong Geun Seong, Jeremy C. Lewis, John A. Matteson, Erica Craddock, Ulises Martinez, Harshul Thakkar, Angelica D. Benavidez, Kathryn A. Berchtold, Rajinder P. Singh

PII: S0008-6223(22)00119-1

DOI: https://doi.org/10.1016/j.carbon.2022.02.033

Reference: CARBON 17027

To appear in: *Carbon*

Received Date: 30 July 2021

Revised Date: 7 February 2022

Accepted Date: 13 February 2022

Please cite this article as: J.G. Seong, J.C. Lewis, J.A. Matteson, E. Craddock, U. Martinez, H. Thakkar, A.D. Benavidez, K.A. Berchtold, R.P. Singh, Polybenzimidazole-derived carbon molecular sieve hollow fiber membranes with tailored oxygen selective transport, *Carbon* (2022), doi: https://doi.org/10.1016/j.carbon.2022.02.033.

CRediT authorship contribution statement

Jong Geun Seong: Conceptualization, Investigation, Data curation, Writing - original draft, Writing - review & editing. **Jeremy C. Lewis**: Investigation, Data curation, Writing - review & editing. **John A. Matteson**: Investigation. **Erica Craddock**: Data curation. **Ulises Martinez**: Data curation, Writing - review & editing. **Harshul Thakkar**: Investigation. **Angelica D. Benavidez**: Data curation. **Kathryn A. Berchtold**: Conceptualization, Writing - review & editing. **Rajinder P. Singh**: Conceptualization, Writing – review & editing, Funding acquisition, Project administration, Supervision, All authors read and contributed to the manuscript.

Graphical Abstract

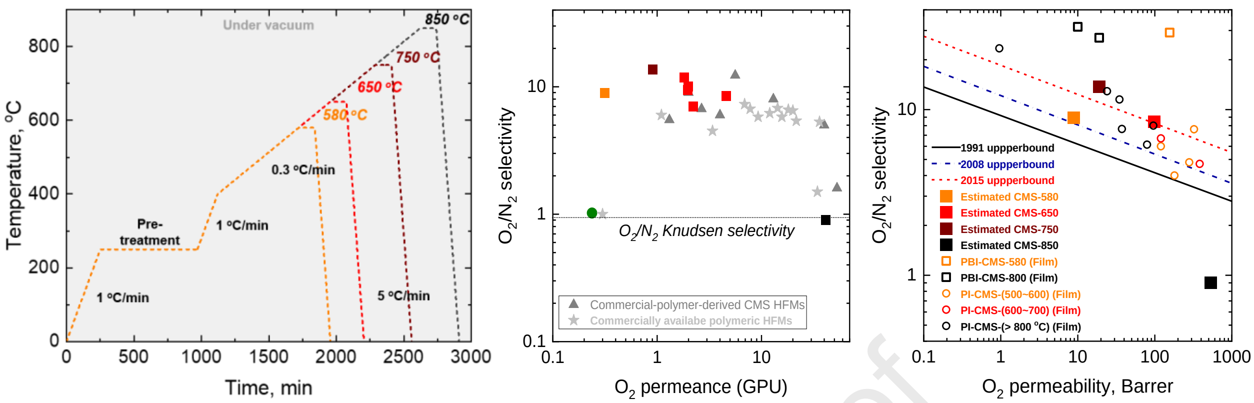

Polybenzimidazole-derived carbon molecular sieve hollow fiber membranes with tailored oxygen selective transport

Jong Geun Seong[a,1], Jeremy C. Lewis[a,1], John A. Matteson[a], Erica Craddock[a], Ulises Martinez[a], Harshul Thakkar[a], Angelica D. Benavidez[b], Kathryn A. Berchtold[a], Rajinder P. Singh[a,*]

[a]*Materials Physics and Applications Division, Los Alamos National Laboratory, Los Alamos NM 87545, United States*

[b]*Department of Chemical and Biological Engineering and Center for Microengineered Materials, University of New Mexico, Albuquerque, NM, 87131, United States*

[1]These authors contributed equally to this work

*Corresponding author: rsingh@lanl.gov (R. P. Singh)

Abstract

Polymer membrane carbonization is a promising strategy to obtain carbon molecular sieve (CMS) membrane materials with tailorable cavity size distributions for high gas selectivities beyond that attained from traditional polymer membrane materials. Despite their already demonstrated exceptional separation performance characteristics for several gas separation applications (e.g. CO_2/CH_4 and H_2/CO_2), further development of CMS membranes having high O_2/N_2 perm-selectivity for energy-efficient high-purity O_2 production has proven challenging. Herein, we explore CMS hollow fiber membranes (HFMs) derived from highly rigid and tightly-packed polybenzimidazole (PBI) materials. Nearly defect-free PBI-derived CMS HFMs were fabricated and evaluated for O_2/N_2 separation performance for the first time. The micro-structural and O_2 selective gas separation characteristics of PBI-CMS HFMs pyrolyzed at different pyrolysis conditions were intensively studied. With rigorous carbonization protocol optimization, we obtained highly O_2 permselective PBI-CMS HFMs having O_2/N_2 selectivities approaching 14, enabling high purity O_2 production. The PBI-CMS HFM O_2/N_2 separation performance dependence on operating conditions (e.g. temperature and feed pressure) are reported.

Keywords: carbon molecular sieve (CMS) membrane; hollow fiber membrane (HFM); polybenzimidazole (PBI); oxygen enrichment; gas separation.

1. Introduction

The demand for high purity oxygen (90-95%) and oxygen-enriched air (OEA) is ever increasing for use in power production and numerous other industrial processes (e.g. steel, cement, aluminum, and copper) in a push to improve overarching process energy efficiencies and to reduce environmentally harmful gas emissions [1, 2]. Taking an example of a steel production process, sinter obtained from the metallurgical coal, lime, and oxygen participates in the reaction of producing steel and oxygen composition ratio during the production can directly dictate process efficiency [3]. Additionally, calcination of limestone is one of the main processes of producing cement and it also causes carbon emission [4]. Thus, integration of oxygen enrichment process into the existing cement production is now considered to be an alternative to capture carbon without the volume penalty of air that has been challenging in oxy-fuel combustion [4]. Similarly in solid fuels (e.g. coal, biomass) gasification processes, combustion in O_2 or OEA environments at aluminum [5] or copper [6] production also improves overall process efficiency, reduces pollutants emissions and downstream operations costs including those associated with CO_2 capture [7]. In concert with the modular (1-5 MWe) gasification-based power generation with near-zero CO_2 emissions approach, an energy efficient modular air separation technology for O_2 production is essential to realize low cost and high level of operational efficiency.

Cryogenic distillation is the industry standard for large scale (>300 tons/day) high purity (> 99%) O_2 production [1]. However, cryogenic technologies for air separation are energy intensive due to their high thermal inefficiencies and are economical only at large scales. Pressure swing adsorption (PSA) methods for air separation typically produce ca. 95% purity O_2 and are suitable for small to medium scale applications, however they require large sorbent volumes due to their low perm-selectivity [1]. The start-up/shut-down times for both cryogenic and PSA-based systems are long, an undesirable characteristic for modular air separation units (ASUs).

Owing to their small foot-prints, on-demand operation, facile start-up/shut-down, and scalability, membrane-based air separation technology is attractive for the modular scale gasification application [8-14]. Commercially available polysulfone (PSf), cellulose acetate (CA) and polyimide (PI) membranes are currently used at industrial scale for air separations. However, low O_2/N_2 perm-selectivity ($\leq$ 10) of polymer membrane materials disrupts simultaneous achievement of high O_2 purity at high stage cut and pressure ratio of 5-10 for energy efficient air separation operation [2, 15-22]. In addition, the polymeric membranes encounter gas permeability and perm-selectivity trade-off relationship hampering development of high perm-selectivity and throughput membrane-based air separation systems [23, 24]. A significant improvement in O_2/N_2 perm-selectivity (>10) is required for energy efficient high purity O_2 production with membrane separation technology. To the best of our knowledge, the only membrane materials developed to-date with demonstrated O_2/N_2 selectivities of greater than 10 are some mixed matrix membranes (MMM) or polymeric membranes bearing metal complexes [25], facilitated transport membranes (FTM) and dense ceramic membranes, *e.g.*, ion transport membranes (ITM) or oxygen transport membranes (OTM) [26-28]. However, interfacial compatibility of additives with polymers or additive aggregation behaviors in polymers has been challenging in MMMs [29, 30]. FTMs suffer long-term stability issues including O_2 carrier loss, and CO_2 and water induced oxidation impeding their industrial deployment [31]. Dense ceramic membranes have both high capital and operating costs driven by their materials of composition, manufacturing requirements, and their mandated operation at elevated temperature, > 600 °C. Additionally, poor mechanical stability, difficult module manufacturing and degradation in CO_2 or low partial pressure O_2 prevent dense ceramic membrane industrial deployment [27].

Polymer-derived carbon molecular sieve (CMS) materials are an emerging class of the membrane material with the potential to overcome the permeability-selectivity limitations of polymer membranes [32, 33]. CMS membranes are fabricated via controlled polymer membrane pyrolysis at elevated temperatures (550 to 900 °C). Polymer pyrolysis induces precursor chain cleavage and aromatization leading to formation of rigid and highly disordered sp^2 planar structures. Correspondingly, slit-like and hourglass-shaped pore morphologies are introduced into the CMS membranes during controlled pyrolysis which significantly improves their gas perm-selectivity characteristics. Since the thermal response to the inter-chain configurations of parental polymer precursors regulates the degree of chain scissions and rearrangement, a rigorous selection of polymer precursors for the CMS membrane formations is crucial. There have been myriads of exploration studies on establishing the physicochemical and transport properties relationships between polymer precursors and resulting CMS membranes [34-37]. PI derived CMS (PI-CMS) membranes have received the most attention for gas separation applications. It is hypothesized that the PI rigidity and superior thermal and chemical stability provide opportunities for the desired sp^2 planar structures formation upon pyrolysis resulting in good separation performance [36]. With CO_2/CH_4 selectivities ranging from 96 to 263 demonstrated, PI-CMS membranes are transitioning to industrial R&D for application in natural gas processing [38, 39]. Despite the excellent performance achieved for natural gas application, PI-CMS membranes have not been realized for O_2 or OEA applications [16].

The starting polymer properties, including their molecular structure and inter- and intra-molecular chain packing characteristics ultimately drive the separation characteristics of the resultant polymer-derived CMS membranes post-pyrolysis [16]. Therefore, we believe polybenzimidazole (PBI)-based molecular sieve membrane materials are a promising class of precursors for further developing CMS membranes with improved separation performance characteristics for O_2 and OEA application. The tightly packed, straight chain molecular structure together with the extensive stacking and hydrogen bonding which imparts exceptional molecular sieving characteristics in PBI materials is anticipated to produce CMS membranes having improved separation performance over their PI-based counterparts. Hosseini *et al* [34, 35] explored PBI and PBI/PI blends to obtain CMS membranes. They reported O_2/N_2 selectivities as high as 32 for PBI-derived CMS flat-sheet membranes. Similarly, Heydari and Pirouzfar [37] reported that PBI/PI blends having 90 wt% or higher PBI content resulted in PBI-CMS flat-sheet membranes having O_2/N_2 perm-selectivity of ca. 29. These studies clearly indicate the unprecedented O_2/N_2 perm-selectivity of the PBI-derived CMS membranes.

In this effort, preparation and evaluation of PBI-derived CMS hollow fiber membranes (HFMs) are reported for the first time to establish their applicability for commercial air separations. Our team's extensive experience in fabricating high performance PBI HFMs optimized for gas separation is leveraged [40]. To the best of our knowledge, there has been no report on PBI-derived CMS HFMs for gas separation application, particularly in O_2/N_2 separation applications. The influences of pyrolysis protocols, and operating conditions (pressure and temperature) are also investigated to understand and optimize gas transport mechanism of PBI-CMS HFMs.

2. Experimental

2.1. Materials

Poly(5,5′-benzimidazole-2,2′-diyl-1,3-phenylene) was used as polymer precursors in this study. A 26 wt% Celazole® PBI solution in dimethyacetamide (DMAc) with 1.5 wt% lithium chloride (LiCl) serving as a phase stabilizer was provided by PBI Performance Products Inc., (Charlotte, NC) and was used for the HFM preparations. DMAc (Fisher Scientific, HPLC grade), acetonitrile (ACN, Fisher Scientific, HPLC grade), acetone (Fisher Scientific, HPLC grade), and hexane (Fisher Scientific) were used as received. The deionized (DI) water used in this study was produced by a Barnstead™ E-Pure™ system (Thermo Fisher Scientific Inc.) with a resistivity of 18 MΩcm.

2.2. Preparation of polybenzimidazole (PBI) hollow fiber precursor membranes

PBI polymeric HFMs (Precursor PBI HFMs) were fabricated *via* non-solvent induced phase separation using a dry-jet wet spinning process, utilizing optimized fabrication methods identified in our previous work [40-42]. The spinning parameters and solution compositions selected to obtain asymmetric HFMs with a thin selective layer on shell side and porous support layer are summarized in Table 1. The spinning dope was prepared by diluting the as-received dope with ACN and DMAc in a high speed centrifugal mixer (AR-250, Thinky Inc.). Syringe pumps (Teledyne Isco, Inc.) were used to deliver the dope and bore fluids to the annulus and inner tube, respectively, of a tube-in-orifice spinneret. The nascent hollow fiber passed through the spinneret, freely fell into an external coagulation bath and was collected on a rotating take-up drum submerged in the coagulation bath. The collected fibers were then immersed in DI water for 24 h to complete the coagulation and remove residual solvent followed by sequential solvent exchange with acetone and hexane for 12 h each. The fibers were then dried in ambient air and stored at ambient conditions prior to use.

Table 1. Summary of spinning parameters for Precursor PBI HFM preparations.

Parameter	Value
Dope concentration (wt%)	PBI/LiCl/ACN/DMAc (18/1/24/57)
Bore fluid (vol.%)	ACN/DMAc (85/15)
Outer coagulant	H_2O
Dope and bore fluid flow rate (ml/h)	10 and 30
Air gap distance (cm)	0.5
Spinneret dimensions (μm)	ID1/OD1/ID2 (203/305/508)
Take-up speed (m/min)	2.54

2.3. Pyrolysis of PBI hollow fiber precursor membranes

PBI-derived CMS HFMs were fabricated under varied, controlled pyrolysis conditions. Precursor PBI HFMs with average length of 60 mm were placed in middle of a three-zone tubular furnace (Lindberg Blue M HTF5534C; Thermo Scientific, Inc.). Given that O_2 content present in the pyrolysis atmosphere influences the separation performance of the resulting CMS membranes [43], the tubular furnace was evacuated and purged with ultrahigh purity (UHP 99.999%) N_2 at least three times to reduce O_2 concentration in the furnace to a level below 10 ppm as measured using an O_2 trace analyzer (Watchdog O_2 tracer, Advanced Micro Instruments, Inc.). After purging with N_2, the tubular furnace was evacuated by < 30mmHg using a turbo pump (TSU 071 E, Pfeiffer Vacuum, Inc.) and pyrolysis was conducted following the pyrolysis profiles presented in Fig. 1. The PBI HFMs were pre-treated for 12 h at 250 °C to remove trace residual solvent and/or water that may have been sorbed during the fiber spinning operation. Following pre-treatment the fibers were heated to 400 °C at a ramp rate of 1 °C/min followed by an additional heating step at a reduced ramp rate (0.3 °C/min) to the target temperature. All samples were held at their target temperature for 2 h prior to cooling. The final pyrolysis temperatures were varied from 580 to

850 °C in this study. The resulting PBI-CMS HFMs are denoted as CMS-X where X indicates target temperature.

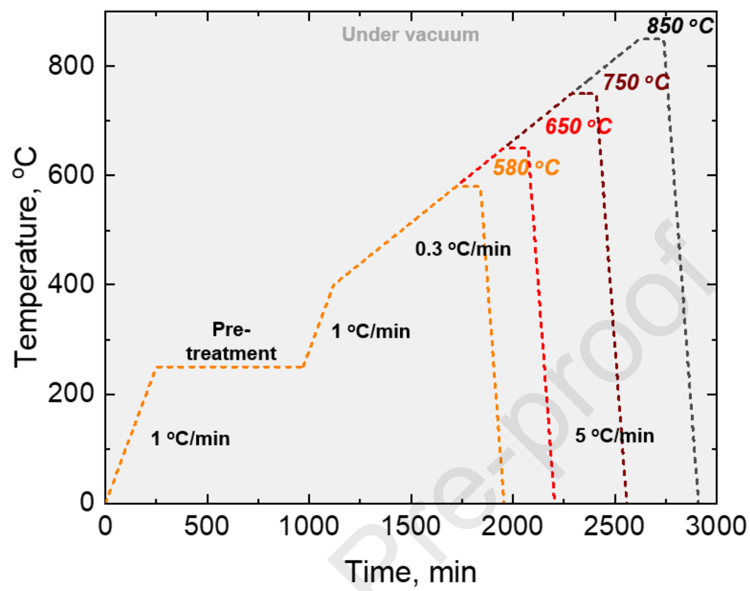

Fig. 1. Pyrolysis temperature profiles used for fabricating PBI-CMS HFMs in this study.

2.4. Characterizations

Extensive thermal, structural, morphological, and micro-structural characterization of the PBI-CMS HFMs were performed. Thermo-gravimetric analysis (STA-650; Hitachi) was performed on Precursor PBI to determine thermal stability and to compare its thermal stability with other polymeric materials reported in literature for CMS membrane formation. To precisely determine its thermal stability and weight loss at the given pyrolysis temperatures, Precursor PBI was heated up at 250 °C for 12 h which is the same condition as pre-treatment was carried out prior to the pyrolysis of Precursor PBI as shown in Fig. 1. Then Precursor PBI was further heated up to 1,000 °C with a ramping rate of 5 °C min $^{-1}$.

Molecular structural changes occurring with the transition from PBI polymeric precursors to PBI-CMS membranes were investigated with Fourier transform infrared (FTIR) spectroscopy.

FTIR spectra were obtained using a FTIR spectrometer (Nicolet model 6700) equipped with an attenuated total reflection (ATR) accessory with a single bounce ZnSe crystal (PIKE technologies VeeMAX III).

XPS measurements were performed on a Kratos Ultra DLD spectrometer using a monochromatic Al Kα source operating at 150 W (1486.6 eV). The operating pressure was 2 x 10^{-9} Torr. Charge compensation was accomplished using low-energy electrons. All spectra were charged referenced by adjusting the C 1s region to 285 eV. High-resolution C 1s and N 1s spectra were acquired at a pass energy of 20 eV. XPS data was processed using Casa XPS software. A linear background subtraction was used for the quantification of the C 1s and N 1s regions.

Raman spectroscopy characterization was performed to monitor changes of disordered carbon and graphitic structures in PBI-CMS HFMs with temperature, using a WITec Alpha 300R confocal Raman spectrometer and an EMCCD detector with a 532 nm excitation wavelength.

Wide angle X-ray diffraction (XRD) analysis was also conducted to further study crystal structure of the PBI and PBI-CMS materials. XRD diffractograms were obtained at 2θ angles ranging from 5° to 60° with a scanning speed of 0.8° min^{-1} using a diffractometer with Cu Kα radiation (1.5418 Å) and a graphite diffracted beam monochromator (Siemens D5000). The diffractograms were analyzed using JADE XRD analysis software (Materials Data Inc.). The obtained XRD intensity can be affected by sample preparation, preferred orientation of diffracting domains, and sample size and thus each sample cut into 2cm long was placed at the same direction and position with regards to the bean monochromator.

Morphological analysis of Precursor PBI and PBI-CMS HFMs fabricated in this study was conducted using a scanning electron microscope (FE-SEM; Inspect F, FEI Company Inc.). All HFMs were fractured in liquid N_2 and coated with a gold conducting layer deposited using a precision etching coating system (Model 682; Gatan Inc.). ImageJ software was used for determining the dimensional properties including outer diameter (OD), inner diameter (ID), and wall thickness (WT).

Skeletal density investigation was performed using a pycnometer (AccuPyc II 1340, Micromeritics Inc). Five repeat measurements were performed on each sample and the average values with the standard deviation of less than 0.001 g cm^{-3} is reported here.

2.5. Gas separation characteristics

Ideal O_2 and N_2 permeation properties of Precursor PBI and PBI-CMS HFMs were measured using a constant-volume/variable-pressure method. The HFMs were installed in stainless steel (SS) membrane housings with one end of the fiber attached to a SS hypodermic needle (inserted in the fiber end) and other capped off using PBI dope as a sealant [41] for outside-in gas flow configuration [feed on shell side and permeate on bore side]. During the permeation experiments, the feed flowrate and pressure were controlled using mass flow controllers and back pressure regulator connected to the feed inlet and outlet ports, respectively. The permeate side was evacuated using a turbo vacuum pump (Pfeiffer Vacuum TMU 064 70l s^{-1}, Asslar, Germany). The upstream and downstream pressures were measured using high accuracy (±0.25% FS) pressure transducers (MKS Instruments, Inc.). All gas permenace data reported here were recorded after membrane pre-heating at 180 °C for at least 6 h with N_2 flow on the feed side and vacuum on permeate side to remove byproducts originated from the pyrolysis reaction and/or trapped water molecules.

The pressure normalized gas flux (*P/l*), i.e., gas permeance, was calculated from the slope of permeate pressure change as a function of time using Eq. (1);

$$P/l = \frac{dp}{dt}\left(\frac{VT_0}{P_0 T A \Delta p}\right) \quad (1)$$

where dp/dt (mmHg/s) is the pressure change at steady-state, V is the volume at the downstream (ca. 60 cm^3 in this study), T (K) is operating temperature, Δp is differential pressure across the HFM, T_0 and P_0 are standard temperature and pressure, respectively, and A is nominal membrane surface area. The HFM surface area ranged from 0.4 to 0.6 cm^2 for all HFMs evaluated in this study as calculated using the OD measured from the SEM analysis. The reported gas permeances were an average of at least three measurements. The uncertainty in the data is 5% or less based on three repeat permeance measurements for each sample. The ideal O_2/N_2 perm-selectivity was calculated by taking the ratio of the gas permeances.

The influence of feed pressure and operating temperature on the gas separation properties were also studied by varying the feed pressure and membrane temperature from 600 to 900 mmHg (i.e., 1.03 to 1.55 bar) and 5 to 100 °C, respectively. The feed pressure range is slightly above the atmospheric pressure (Los Alamos, NM, USA atmospheric pressure ca. 580 mmHg) which is consistent with the vacuum permeate configuration reported to be the most energy efficient for air separations [2]. Gas transport through membranes is a thermodynamic phenomenon and thus, gas permeance can be expressed by the Arrhenius equation, Eq. (2). The influence of temperature on gas transport of the PBI-CMS HFMs was quantitatively determined by calculating activation energy of permeation (E_p).

$$P/l = P_0 exp\left(-E_p/RT\right) \quad (2)$$

where P_0 is the front factor, R is the ideal gas constant and T is the absolute temperature (K).

3. Results and discussion

3.1. Thermal characteristics of PBI precursor membranes

The thermal characteristics of the polymer precursor utilized play an important role in determining the optimum pyrolytic conditions. The polymer precursor weight loss profile as a function of temperature guides the target pyrolysis temperature which influences the mechanical and dimensional characteristics of the resulting CMS membranes. A TGA thermogram of the PBI polymer precursor is presented in Fig. 2. A weight loss of < 1 wt% was observed for precursor PBI at temperatures up to ca. 513.5 °C. The degradation onset temperature for PBI, defined as the intersection of tangential lines drawn in the vicinity of the degradation point, was ca. 548 °C. The weight loss increased from 3.6 to 22.1% as temperature increased from 580 to 850 °C.

The weight loss at 850 °C for PBI was ca. 22.1%, which is significantly lower than standard PI-based CMS precursor materials (e.g., P84® PI: ca. 34% at 900 °C [44], cross-linkable PI: ca. 50% at 900 °C [45], and polyetherimides: ca. 50% at 900 °C [46]), and other polymeric materials studied for CMS membranes (cellulose acetates: ca. 80% at 600 °C) [47] and polyacrylonitriles: ca. 100% at 680 °C [48]). The low weight loss characteristics of PBI are highly desirable as they will aid in the retention of the dimensional and morphological features of the precursor membrane during pyrolysis and correspondingly, increase the tailorability of the produced CMS membrane properties and improve manufacturability. Based on the thermal characteristics of PBI; 580 °C, 650 °C, 750 °C and 850 °C were selected as the target pyrolysis temperatures in this work. PBI-CMS HFMs pyrolyzed at different temperatures were mechanically flexible as demonstrated in Fig. 3 by bending to a diameter of < 25 mm around a United States Quarter. It is expected that chemical (residual N-groups and their structure), structural (graphitic vs. disordered carbon phases) and morphological (support layer pore structure densification at elevated temperatures) changes in

PBI-CMS HFMs as a function of pyrolysis temperature will enable tailoring of gas transport characteristics.

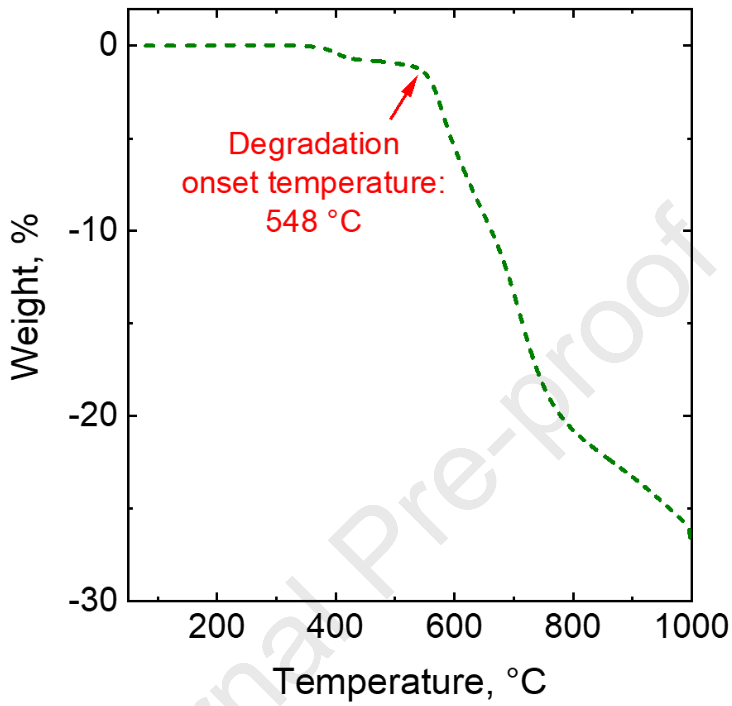

Fig. 2. TGA thermogram of PBI. The degradation onset temperature is determined by drawing tangential lines on the weight loss curve in the vicinity of the degradation point. The entire run for this thermo-gravimetric analysis is available in Fig. S1 in the supplementary information.

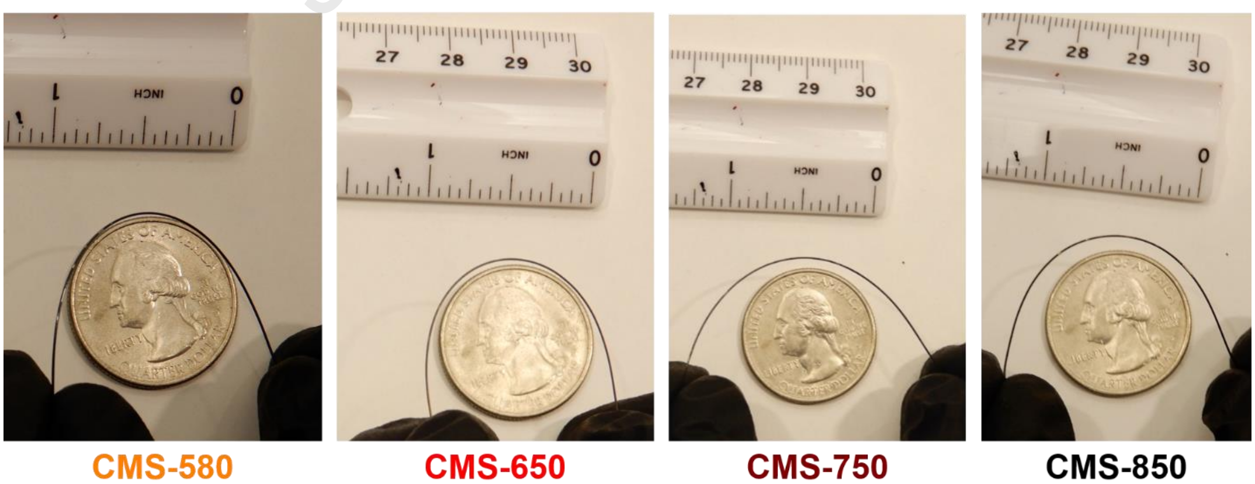

Fig. 3. Mechanical flexibility of PBI-CMS HFMs fabricated in this study as demonstrated by bending to < 25 mm diameter (around a United States Quarter).

Table 2. Thermal, chemical, structural and dimensional characteristics of PBI and PBI-CMS HFMs.

		Precursor PBI	PBI-CMS HFMs			
			CMS-580	CMS-650	CMS-750	CMS-850
Weight loss		-	3.6	9.1	18.4	22.1
Atomic concentration (%) by deconvolution of XPS N 1s spectra	C=N at 399.05 eV	39.9	35.8	35.9	34.3	17.0
	C-N at 400.90 eV	60.1	45.8	44.8	34.0	35.4
	N pyridinic at 398.71 eV	-	8.3	4.1	6.8	6.0
	N pyrrolic at 400.20 eV	-	10.1	4.4	9.7	26.9
	N graphitic at 401.83 eV	-	-	10.9	15.2	14.8
Selective layer thickness[a] (µm)		0.3	28±6	25±4	21±4	13±2
Dimensional parameters	Outer diameter (OD, µm)	488±25	352±8	332±23	321±7	318±8
	Inner diameter (ID, µm)	405±26	296±8	283±20	276±6	270±5
	Wall thickness (WT, µm)	42±8	28±6	25±4	21±4	18±6
	Wall thickness ratio[b] (WTR, %)	17.1	15.9	14.7	14.1	15.1
% shrinkage[c]	OD	-	27.8	32.0	34.2	34.9
	ID	-	26.8	30.0	31.7	33.3
Skeletal density (g cm^{-3})		1.21	1.64	1.84	1.86	1.62

[a] as obtained from SEM image analysis
[b] WTR = (OD-ID) / OD X 100
[c] % Shrinkage = ((diameter of polymeric HFM)-(diameter of pyrolyzed HFM)) / (diameter of polymeric HFM) x 100

3.2. Structural properties of PBI-CMS membranes

The FTIR spectra obtained on PBI and PBI-CMS samples for the molecular structural characterization as a function of pyrolysis temperature are presented in Fig. 4. The characteristic PBI absorption peaks were clearly evident in the FTIR spectrum of Precursor PBI sample. These peaks were assigned to stretching vibration of N-H hydrogen bonding between PBI polymer chains (3139 cm^{-1}), aromatic C-H stretching (3050 cm^{-1}), C=C and C=N stretching of benzimidazole moieties (1602 cm^{-1}), in-plane ring vibration of imidazole ring (1445 cm^{-1}), and C-C stretching (1400 cm^{-1}) [49, 50]. All of the PBI characteristic peaks were absent in the resultant carbon samples except for the sample pyrolyzed at 580 °C (CMS-580). In addition, the peak at 2225 cm^{-1} was only observed in CMS-580, which represents hydrogen cyanide (HCN) or cyanogen [51, 52] resulting from imidazole rings cleavage, an intermediate step to PBI carbonization. This indicates pyrolysis at 580 °C is unable to achieve complete carbonization of PBI in 2 h.

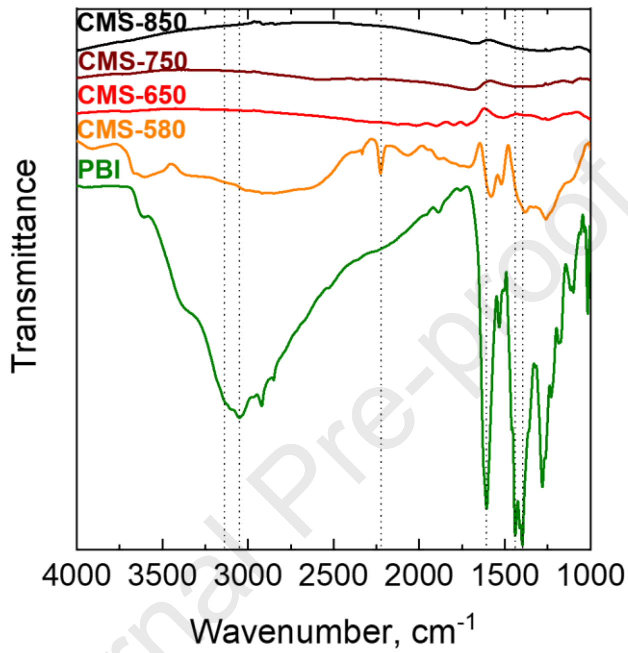

Fig. 4. FT-IR spectra of Precursor PBI and its carbon products formed at pyrolysis temperatures ranging from 580 to 850 °C. Dashed lines are presented to guide the eye.

XPS characterization helped further elucidate changes observed in the pyrolytic carbon structures of PBI-CMS HFMs as a function of temperature. As depicted in Fig. 5, C ls and N 1s spectra are shown for CMS-580, CMS-650, CMS-750, and CMS-850. The peak at binding energy 284.8 eV in the C 1s spectra was assigned to the graphitic-like sp^2 bonded carbon [53]. This sp^2 carbon peak for all PBI-CMS HFMs was higher than the peak for sp^3 carbon (285.5 eV), except for CMS-580 which still had a significant amount of unpyrolyzed PBI, as evidenced from the aforementioned FTIR data analysis. It is evident that pyrolytic conversion of PBI into PBI-CMS was carried out at 580 °C and the conversion ratio was increased with increasing pyrolysis temperature.

With regards to the N 1s spectra, presented in Fig. 5 and Table 2, the main characteristic is the transformation of the N in the C=N and C-N bonds in the benzimidazole functional group of the PBI polymeric backbone into pyridinic, pyrrolic, or graphitic N incorporated into the lattice of the sp^2 carbons. In particular, the graphitic N only formed at temperatures higher than 650 °C, while the major PBI decomposition was observed at 850 °C with a significant amount of C=N moieties were converted into pyrrolic N. As pyrolytic carbonization proceeds with increasing temperature, more C=N and C-N bonds participated in the transformation into N pyridinic or pyrrolic carbons followed by N graphitic carbons, which is consistent trend in other carbon molecular sieve membranes derived from N-containing polyimide precursors [53].

Characterization of the degree of graphitization and defects of carbon structures is typically achieved using Raman spectroscopy. For carbon-structures, the degree of graphitization increases with increasing pyrolysis temperature. However, for N-containing polymeric precursors, it has been reported that the transformation of C=N and C-N bonds in the benzimidazole rings of Precursor PBI into pyridinic, pyrrolic, and graphitic nitrogen in the sp^2 lattice of the pyrolyzed carbon backbone induces intrinsic defects [54]. Thus, Raman spectroscopy obtained for all PBI-CMS HFMs, shown in Fig. 6, represents both of these phenomena. All spectra showed two distinct peaks, D peak at 1330~1340 cm^{-1} and G peak at 1560~1570 cm^{-1}, which are assigned to disordered and defective structure of graphite (D peak), and ideal and regular graphitic vibration (G peak), respectively [55]. The collected data shows that relative intensities of I_D/I_G were higher than 1 with a small maximum at 750 °C. The decrease in I_D/I_G observed at 850 °C is most likely due to an increase in graphitic carbon in combination with a decrease in overall N moieties. Overall, these results are in well agreement with the XPS results shown in Fig. 5.

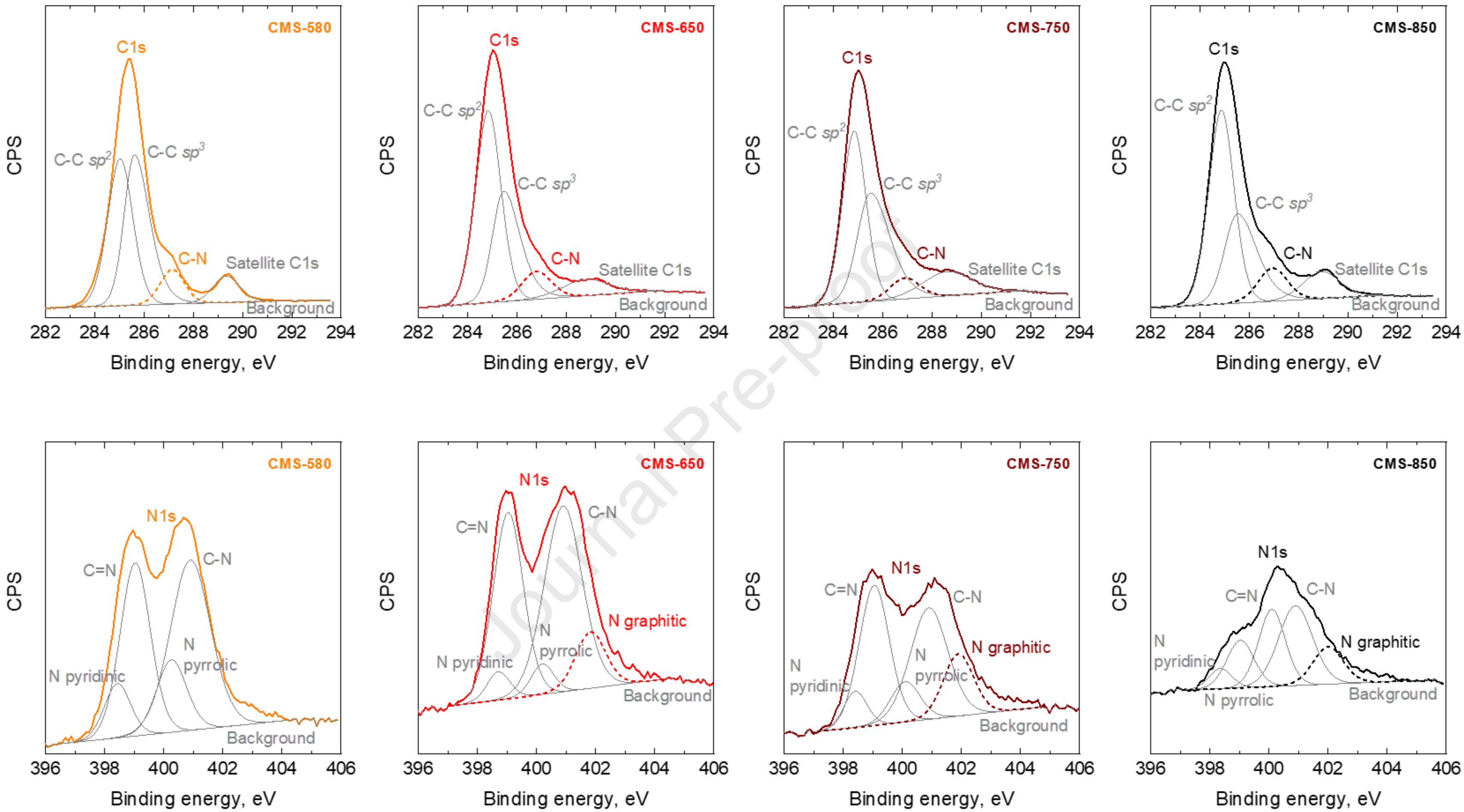

1
2 **Fig. 5**. Deconvoluted C1s (top row) and N1s XPS spectra of all PBI-CMS HFMs in this study.

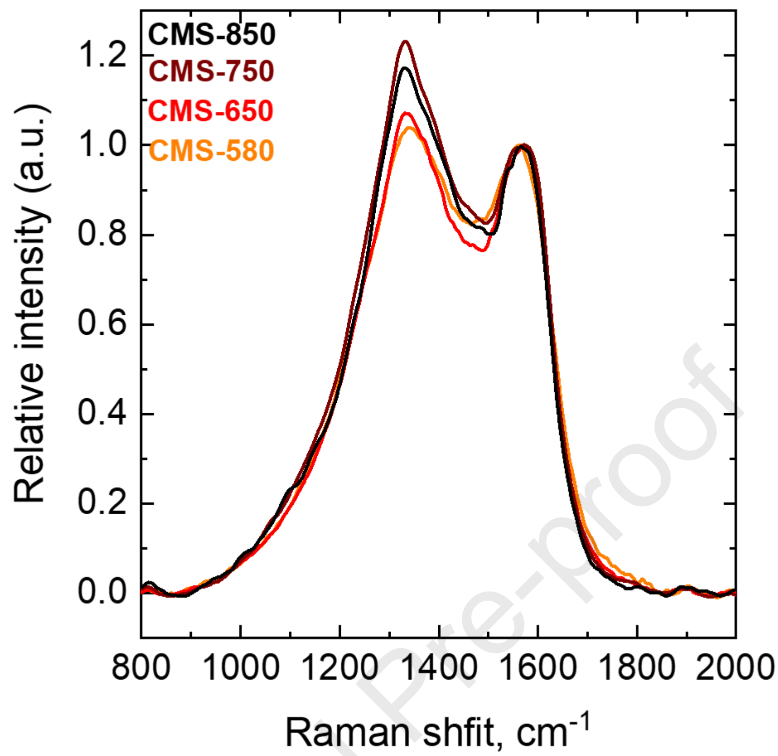

Fig. 6. Raman spectra of all PBI-CMS HFMs in this study.

3.3. Morphological characterization

Extensive surface and cross-sectional SEM images were obtained to study the dimensional characteristics and structural morphologies of PBI and PBI-CMS HFMs. As shown in Fig. 7, Precursor PBI HFM (pre-pyrolysis) exhibited an asymmetric morphology with a distinct selective layer of ca. 300 nm on the shell side supported by a porous interconnected support layer. After pyrolysis, complete collapse of the porous support layer was observed for all the PBI-CMS HFMs resulting in a symmetric morphology, which is consistent with CMS HFMs reported elsewhere [38, 39, 47, 56]. The presence of isolated pinholes defects was clearly evident on the surface and throughout the fiber wall with more prevalent presence near the inner surface of the fibers. Since the pinholes were isolated and SEM images did not indicate interconnectivity among pinhole defects, the selective layer of the PBI-CMS HFMs was considered equal to the wall thickness which decreased from 28 to 13 μm as a pyrolysis temperature increased from 580 to 850 °C, respectively.

Quantitative analysis of the dimensional changes as a function of pyrolysis temperature are reported in Table 2. The outer diameter (OD) and wall thickness (WT) of CMS-580 were 352±8 μm and 28±6 μm, respectively, exhibiting a decrease of 28% and 32%, respectively in comparison to Precursor PBI (488±25 μm and 42±8 μm). Overall, the fiber OD and ID decreased by 28 to 35% as the pyrolysis temperature increased from 580 to 850 °C. The higher degree of fiber dimensional change as a function of pyrolysis temperature indicates higher degree of densification at elevated temperatures. The PBI HFMs demonstrated significantly lower % shrinkage in OD as compared to other polymer derived CMS HFMs (e.g. cellulose acetate derived CMS HFM fabricated by pyrolysis at 550 °C had ca. 36% shrinkage in OD [47]). This lower % dimensional shrinkage observed in PBI HFMs is an attractive feature for the CMS membrane fabrication.

Change in skeletal density for the obtained PBI-CMS HFMs with pyrolysis temperature was also investigated using He gas pycnometer (Table 2). He gas pycnometry is based on excluding the pore volume which He gas can penetrate and thus it is used as a criteria of accessibility to pores bigger than 2.6 Å [57]. CMS-580 had a skeletal density of 1.64 g cm^{-3} which is consistent with the density of PBI-CMS flat-sheet membranes from the previous report [58]. The skeletal density increased as pyrolysis temperature increased with maximum value at 750 °C. The density of PBI-CMS HFMs was similar to symmetric cellulose-derived CMS HFMs (1.6~1.7 g cm^{-3}) but significantly smaller than non-porous crystalline graphite (2.3 cm^{-3}) [59].

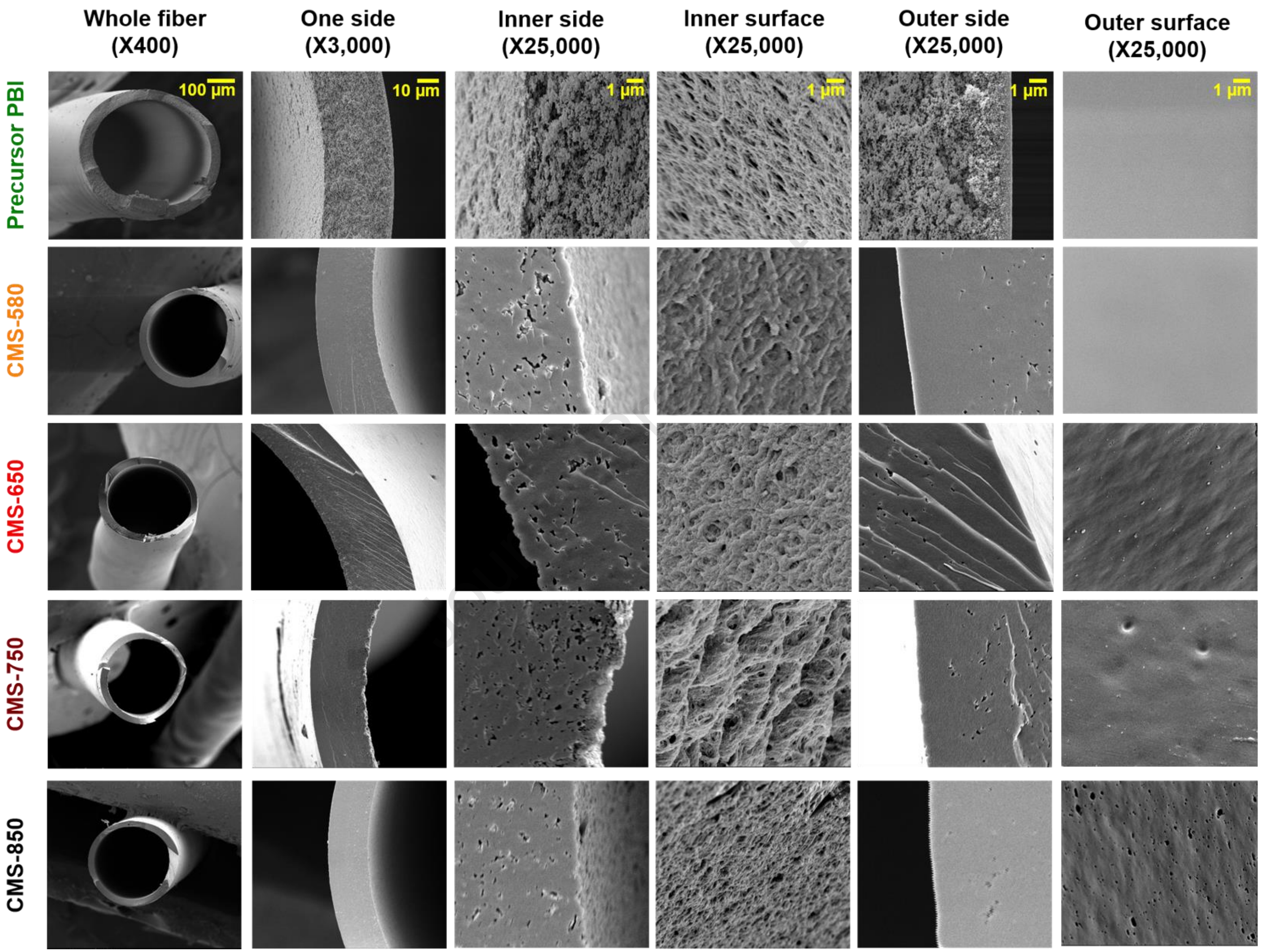

Fig. 7. Representative SEM micrographs of Precursor PBI and PBI-CMS HFMs.

The XRD diffractograms measured for Precursor PBI and PBI-CMS samples as a function of pyrolysis temperature are presented in Fig. 8 and Table 3. Precursor PBI presented a broad diffraction peak located at $2\theta = 22.6^o$ which is consistent with the literature [60]. After pyrolysis, broad peaks in three distinct 2θ zones were observed for all the PBI-CMS samples. First peak at 2θ of ~5^o (zone I), the second peak at a 2θ of 16~24^o (zone II), and the last peak with the smallest intensity at a 2θ of 41~44^o (zone III) were observed. Based on the Bragg equation [61, 62], the peaks in zones I, II and III correspond to distances between diffracting planes of ~ 18 Å, 3.7~5.5 Å, and 2 Å, respectively. The estimated distance range corresponding to the zone II peak comprises the size range corresponding to the O_2 (3.46 Å) and N_2 (3.64 Å) kinetic diameters and correspondingly, is likely a key controlling factor of O_2/N_2 perm-selectivity in PBI-CMS HFMs. In comparison to the CMS membranes derived from other polymeric materials, the *d*-spacing for the peak in zone II observed for the PBI-derived CMS membranes were slightly smaller than the PI-derived CMS materials [63], however, they were larger than the poly (arylene ether ketone)-derived CMS materials [64]. The smaller *d*-spacing characteristics of the PBI-CMS materials are anticipated to enable higher O_2/N_2 perm-selectivity than the PI-derived CMS materials.

The characteristic peak of Precursor PBI at zone II corresponding to a 2θ value of 22.6° shifted towards smaller 2θ value of 19.6° upon pyrolysis at 580 °C indicating an increase in *d*-spacing. However, the PBI-CMS materials prepared at 750 and 850 °C, had main 2θ peaks at a location slightly higher values than that observed for Precursor PBI, which is well agreement with the previously reported literatures [34, 35, 58]. It can be hypothesized that pyrolysis rendered the ordered packing domain in Precursor PBI to be firstly disordered with enhanced *d*-spacings (pyrolyzed at 580 °C) followed by re-organization to render tighter *d*-spacings due to formation of more graphitic structures at pyrolysis temperatures higher than 650 °C as also confirmed by aforementioned XPS and Raman investigations [65]. Interestingly, the estimated *d*-spacings of ~3.8 Å for PBI-CMS pyrolyzed at temperatures higher than 700 °C is comparable to that for a pure graphitic structure [65]. This is also complemented by the existence of a peak at $2\theta > 40^o$ (Zone III) in PBI-CMS materials corresponding to a peak characteristic of the (100) plane of graphite [65]. The intensity of the peak at zone III increased as pyrolysis temperature increased indicating increased graphitization with increasing pyrolysis temperature.

In addition, pyrolysis induced formation of a new peak at $2\theta < 15^o$ (Zone I) which corresponds to a *d*-spacing larger than 6 Å [34] and can be attributed to higher gas permeability of pyrolyzed PBI as compared to Precursor PBI. The tailorable chain packing configurations in the resulting PBI-CMS membranes as function of pyrolysis temperature are anticipated to enable control on the gas separation characteristics, which are discussed in the following section.

Table 3. Peak assignment for Precursor PBI and PBI-CMS samples. Numbers in round brackets represents their intensity values found in Fig. 8 while numbers in square brackets are their respective *d*-spacing values (in Å) obtained from Bragg equation [61, 62]. A schematic illustrating the representative pore sizes in all PBI-CMS HFMs in this study is provided in supplementary information.

	2*θ*	**Comments**	PBI	CMS-580	CMS-650	CMS-750	CMS-850
Zone I	$5^o \sim 10^o$	9 Å < distance between diffracting planes		5.4 (578) [16]	5.2 (976) [17]	5 (779) [18]	5.2 (626) [17]
Zone II	$15^o \sim 30^o$	3 Å < distance < 6 Å	22.6 (1091) [3.9]	19.6 (447) [4.5]	22.2 (465) [4.0]	23.0 (562) [3.9]	23.6 (385) [3.8]
Zone III	$40^o \sim 50^o$	distance < 2 Å		42.3 (169) [2.1]	43.2 (182) [2.1]	43.7 (186) [2.1]	41.4 (141) [2.2]

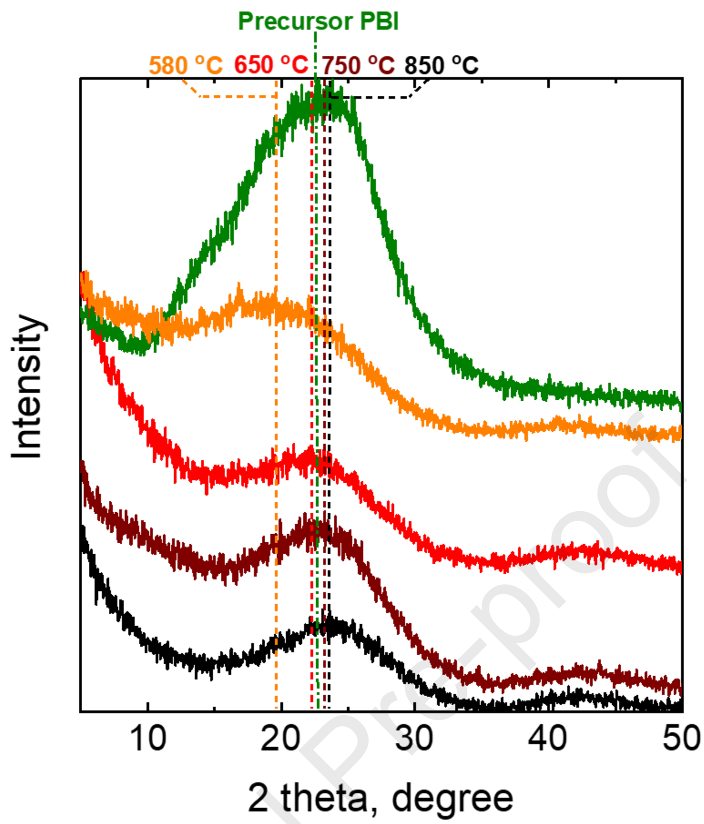

Fig. 8. XRD patterns of Precursor PBI (green-colored) and PBI-CMS samples (CMS-580 (orange); CMS-650 (red); CMS-750 (wine); and CMS-850 (black), respectively). All patterns were obtained by subtracting the background signal (Fig. S2 presented in the supplementary information) and then vertically translated without adjusting intensity for clarity. All dot lines were obtained from 2θ which is centered of the broad peak in Zone II.

3.4. Gas Separation Characteristics

3.4.1. Influence of pyrolysis temperature on gas separation characteristics

The influences of morphological changes and microporous characteristics as a function of pyrolysis temperature on O_2 and N_2 separation characteristics were systemically investigated. These results are summarized in Fig. 9 and Table 4. On basis of the result of relationships between WAXD intensity and pore concentration investigated by Positron annihilation lifetime spectrometry (PALS) under the carefully controlled conditions [66, 67], origin of gas separation characteristic changes in the obtained PBI-CMS HFMs can be correlated to the WAXD result. For reference, Precursor PBI had an O_2 permeance and O_2/N_2 perm-selectivity of 0.2 GPU and 1.0, respectively. After pyrolysis, both the O_2 permeances and O_2/N_2 selectivities improved significantly at all pyrolysis temperatures except 850 °C. The best O_2 permeance and O_2/N_2 perm-selectivity combination of 4.0 GPU and 8.5, respectively, was measured for the PBI-CMS HFMs fabricated at 650 °C.

The PBI-CMS HFM O_2 permeance increased from 0.3 to 4.0 GPU as pyrolysis temperature increased from 580 to 650 °C as presented in Fig. 9 and Table 4. This can be envisaged that the partial carbonization of PBI-580, as evident in the FTIR analysis (Fig. 4), likely contributed to lower O_2 permeance of PBI-580 in comparison to PBI-650. In addition, as discussed in XRD characterization of PBI-CMS (section 3.3), CMS-650 exhibited a larger intensity for 2θ peaks in zone I (representing the distance between diffracting planes > 9 Å), which can also be contributed to its higher O_2 permeance as compared to the CMS-580. It can be hypothesized that decrement in the distance of diffracting planes from 4.5 to 4.0 Å at zone II played a minimal role in controlling O_2/N_2 perm-selectivity of CMS-650 from CMS-580.

As pyrolysis temperature increased from 650 to 750 °C, O_2 permeance decreased from 4.0 to 0.8 GPU and O_2/N_2 perm-selectivity increased from 8.5 to 13.7. This variation in O_2/N_2 perm-selectivity could be explained by comparing zone I and II peaks of XRD diffractograms obtained on the PBI-CMS samples pyrolyzed at 650 and 750 °C. Reduction in the intensity of zone I peak from 976 (650 °C) to 779 (750 °C) could be attributed to decrease in the O_2 permeance. On the other hand, the higher intensity values of peaks in zone II and zone III for sample pyrolyzed at 750 °C may be attributed to higher O_2/N_2 selectivity for CMS-750 as compared to CMS-650. The observed downturn in gas transport characteristics by the influence of collapse in carbon turbostratic structures at higher pyrolysis temperature has been observed previously for the CMS membranes. For example, C_2H_4 permeance and C_2H_4/C_2H_6 perm-selectivity for PI-based CMS HFMs made of Matrimid® changed from 0.27 (C_2H_4/C_2H_6 of 9) to 0.18 GPU (~14) as pyrolysis temperature increased from 650 to 750 °C [56]. Ultem 1000®-derived polyetherimide-based CMS HFMs also presented deduction in CO_2 permeance from 1.66 (650 °C) to 0.69 GPU (800 °C) but improvement in CO_2/CH_4 selectivity from 55 to 69 [46].

Further increase in the pyrolysis temperature to 850 °C led to 1-2 order increase in O_2 permeance but complete loss of O_2/N_2 perm-selectivity. It seems to be contradictable compared to the XRD investigation result. The distance between diffracting planes at zone II for CMS-850 was the smallest in this study and there was a previous report whose O_2/N_2 selectivity pyrolyzed at 800 °C was higher than the one pyrolyzed at 580 °C [35]. It could be attributed to formation of defects in the membrane. The higher permeance but no O_2/N_2 separation performance for CMS-850 can be explained by higher populations of defects or pinholes as observed in the outer surface SEM images in Fig. 7.

To assess practical feasibility of the obtained PBI-CMS HFMs in this study, physical aging response of the selected CMS-750 was explored. CMS-750 was stored in ambient atmosphere for 153 day prior to the exploration. As presented in Table 4, there showed a decrement by 50% in O_2 permeance (from 0.782 to 0.394 GPU) with slight decline in O_2/N_2 selectivity, which is a typical phenomenological result observed in carbon molecular sieve membranes from literature; 69% loss in CO_2 permeance for 30-day-aged 6FDA-DETDA:DABA (cross-linkable PI) CMS HFM [68] and 23% loss in CO_2 permeance for 6FDA:BPDA-DAM (1:1) (PI) CMS HFM stored in 50 psia N_2 for 21 days [33].

This large span in gas separation performance indicates the significant influence of the pyrolysis protocols on the PBI-CMS HFMs. The data obtained indicates that pyrolysis temperature in the vicinity of 650 °C seems to be optimum for achieving the best combination of O_2 permeance and O_2/N_2 perm-selectivity.

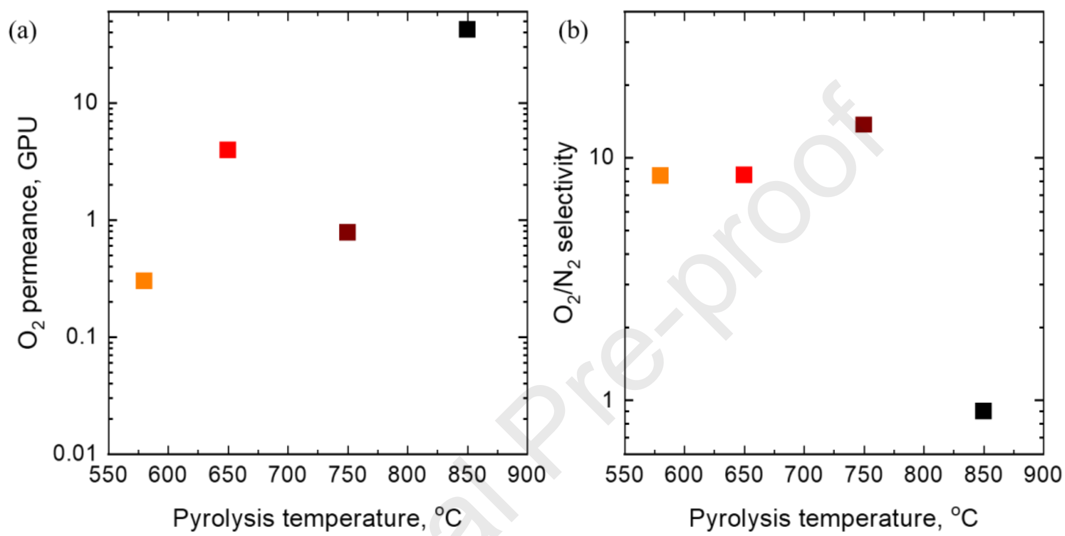

Fig. 9. (a) O_2 permeance and (b) O_2/N_2 perm-selectivity of PBI-CMS HFMs with controlled pyrolysis temperature (CMS-580 (orange); CMS-650 (red); CMS-750 (wine); and CMS-850 (black), respectively). The values reported here are an average of at least three measurements. The standard deviation from the mean is within 5%.

Table 4. O_2 separation performances at 900 mmHg and 25 °C of all PBI polymeric and PBI-CMS HFMs in this study. The values reported here are an average of at least three measurements. The standard deviation from the mean is within 5%.

Sample	**Performance**		**Estimation**
	O_2 permeance [GPU]	O_2/N_2 [-]	Estimated O_2 permeability [Barrer]
PBI	0.204	1.02	0.06
CMS-580	0.303	8.44	8.48
CMS-650	3.964	8.47	99
CMS-750	0.782	13.7	16.4
CMS-750 (153-day-aged)	0.394	10.7	8.27
CMS-850	42.3	0.90	550

Physical aging of PBI-CMS HFMs was evaluated by re-testing CMS-750 after being stored in ambient atmosphere for 153 day. As presented in Table 4, ca. 50% reduction in the O_2 permeance (from 0.782 to 0.394 GPU) was measured with ca. 20% reduction in O_2/N_2 selectivity. The observed physical ageing trend in the PBI-CMS HFMs is consistent with the physical ageing observed for CSM membranes reported previously. CO_2 permeance reduced by 69% in 6FDA-DETDA:DABA (cross-linkable PI) CMS HFM [68] after 30 days and a 23% loss in CO_2 permeance for 6FDA:BPDA-DAM (1:1) (PI) CMS HFM stored in 50 psia N_2 for 21 days was observed [33].

3.4.2. Influence of operating temperature and pressure on gas separation characteristics

The gas transport characteristics of CMS-650 were measured as a function of operating temperature (Fig. 10). Both O_2 and N_2 permeances increased as operating temperature increased from 5 to 100 °C. Correspondingly, O_2/N_2 perm-selectivity of CMS-650 steadily decreased from 12 to 7 as operating temperature increased from 5 to 100 °C. This observed trend in O_2 perm-selectivity as a function of operating temperature was consistent with the activated gas transport mechanism typically observed in molecular sieving materials [61, 62, 69]. The activation energies for permeation (E_p) were calculated at 6.4 and 1.7 kJ/mol for N_2 and O_2, respectively. The difference in E_p between O_2 and N_2 (-4.7 kJ/mol) for CMS-650 is comparable or higher than those reported for the CMS HFMs derived from P84® PI (-2.4 kJ/mol) [44] and CA (-0.9 ~ -4.8kJ/mol) [47]. The higher difference in the E_p between O_2 and N_2 indicates a large variation in the O_2/N_2 separation performances as a function of temperature which provides increased opportunities for process intensification towards designing multi-stage membrane processes for energy-efficient air separations.

The influence of feed pressure on the O_2 separation performances of CMS-650 was also measured at 5 °C (Fig. 11). The O_2 and N_2 permeances were steady with increasing feed pressure from 600 to 900 mmHg. This presents a small pressurization of the feed stream above the atmospheric pressure (ca. 580 mmHg) in Los Alamos, NM consistent with the envisioned feed pressure range of air separation unit primarily relying on the permeate side evacuation to generate driving force for the gas transport. There were no significant differences in O_2/N_2 perm-selectivity as a function of pressure at 5 °C indicating absence of viscous flow transport mechanism. In other words, the HFM was defect-free and functional over the range of envisioned operating conditions.

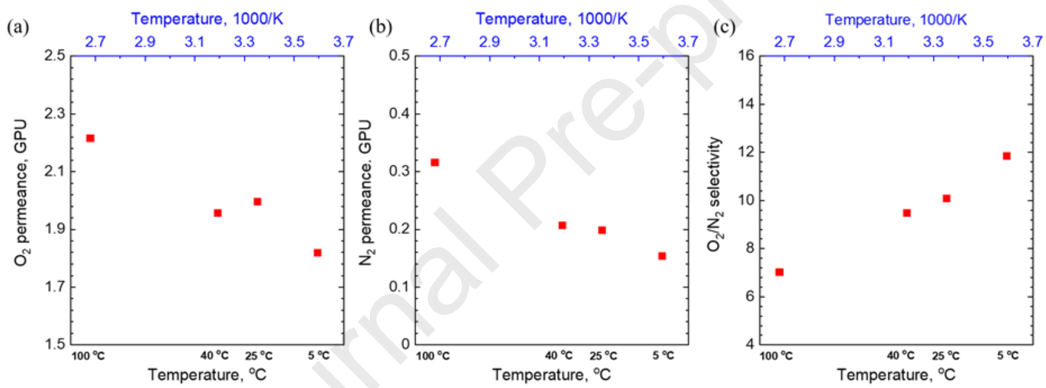

Fig. 10: (a) O_2 permeance, (b) N_2 permeance and (c) O_2/N_2 perm-selectivity dependence on operating temperature for CMS-650. The values reported here are an average of at least three measurements. The standard deviation from the mean is within 5%.

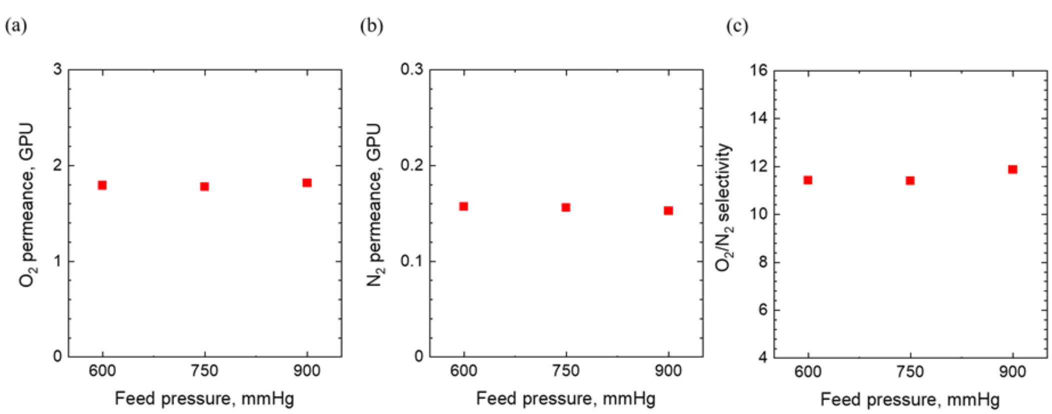

Fig. 11: (a) O_2 permeance, (b) N_2 permeance and (c) O_2/N_2 perm-selectivity dependence on feed pressure measured at 5 °C for CMS-650. The values reported here are an average of at least three measurements. The standard deviation from the mean is within 5%.

3.4.3. Comparison to other polymeric and pyrolytic HFMs

Polymeric HFMs fabricated using commercially available polymeric materials like P84® PI [17], Matrimid® PI [18-20], PSf Udel P-1800 [21] and polyethersulfone Radel A-300 [22] have been extensively studied and industrially utilized for O_2/N_2 separation applications. However, there have been only a few studies on polymer derived CMS HFMs for O_2/N_2 separation applications, including P84® PI [44], Matrimid® PI [19, 38, 70, 71], CA [47] and polyacrylonitriles [48]. Apparently, there has been no report yet on the PBI-CMS HFMs for gas separation applications. The O_2 separation performance of PBI-CMS HFMs developed in this work are compared to the previously reported commercial polymeric and CMS HFMs in Table 5. PBI-CMS HFMs exhibited higher O_2/N_2 perm-selectivities (7.0~13.7) than polymeric HFMs made of commercially available polymers (1.5~8.7), potentially reducing the operating cost [15, 17-22]. PBI-CMS HFMs required lower temperature pyrolysis to achieve comparable or slightly higher O_2/N_2 perm-selectivity than that compared to the CMS HFMs (1.6~12.3) derived from other commercially available polymers [19, 38, 44, 47, 48, 70]. The highest O_2/N_2 perm-selectivity of ca. 13.7 was measured for the PBI-CMS HFM prepared at 750 °C as compared to previously reported the highest O_2/N_2 of ca. 10.0 and 21.0 obtained for Matrimid® PI-based CMS HFMs pyrolyzed at 750 and 900 °C, respectively [71]. In general, higher pyrolysis temperatures (ca. 900 °C) are required to achieve $O_2/N_2 > 10$ in PI-derived CMS membranes as compared to PBI-based CMS membranes. The lower pyrolysis temperature of PBI-CMS HFMs in this study is advantageous towards lower manufacturing costs, lower dimensional shrinkage and better mechanically robustness.

In this work, a high O_2/N_2 perm-selectivity with relatively low O_2 permeances was achieved for the PBI-CMS HFMs, in comparison to the O_2/N_2 separation performances of polymeric and polymer derived CMS HFMs (Table 5). It is due to the complete collapse of the porous support layer during pyrolysis as evident in the SEM images (Fig. 7). The estimated O_2 permeability values for the PBI-CMS HFMs, reported in Table 4 and Fig. 12 were calculated by multiplying O_2 permeances with wall thicknesses measured from SEM images presented in Fig. 7. The estimated O_2 permeability ranged from 8.48 to 99 Barrer for nearly defect-free HFMs as indicated by the O_2/N_2 perm-selectivity of 8 or greater. The O_2/N_2 perm-selectivity characteristics of the PBI-CMS HFMs lie above the 2015 upper-bound trade-off curve for O_2/N_2 recently reported [24]. Apparently that the upper-bound line is a semi-empirical trade-off relationship between gas permeability and gas selectivity observed in polymeric membrane materials, however, it has also been widely used in CMS membranes to intuitively compare membrane performances [34, 35, 72-74]. The previous report on PBI derived CMS flat-sheet membranes showed higher O_2 permeability and O_2/N_2 perm-selectivity than that estimated for the PBI-CMS HFMs of this study [35]. The fabrication procedures for dense-flat sheet membranes and HFMs are drastically different which can drastically influence on the polymer precursor macro-molecular characteristics including polymer packing. The differences in polymer precursor macro-molecular characteristics can be attributed to lower O_2 perm-selectivity measured in this study as compared to flat-sheet membranes. This also indicates that further improvement in O_2/N_2 selectivity can be achieved with intensive understanding of the influence of fabrication conditions on resulting PBI-CMS membranes.

Recently, studies on retaining asymmetric morphology during polymeric HFM pyrolysis have gained much attentions. For example, sol-gel crosslinking prior to pyrolysis endowed Matrimid®-derived CMS HFMs to be 6.5 ~ 10 times higher O_2 permeances than the one without pre-pyrolysis treatment [38]. Similar, pre-pyrolysis treatments are reported for the P84®-based (5.6 GPU, [44]) or CA-based (2.7 GPU, [47]) CMS HFMs to mitigate porous morphology collapse for enhancing

O_2 permeance. Novel methods to mitigate porous morphology collapse during pyrolysis in the PBI-derived CMS HFMs are currently explored and will be reported in near future.

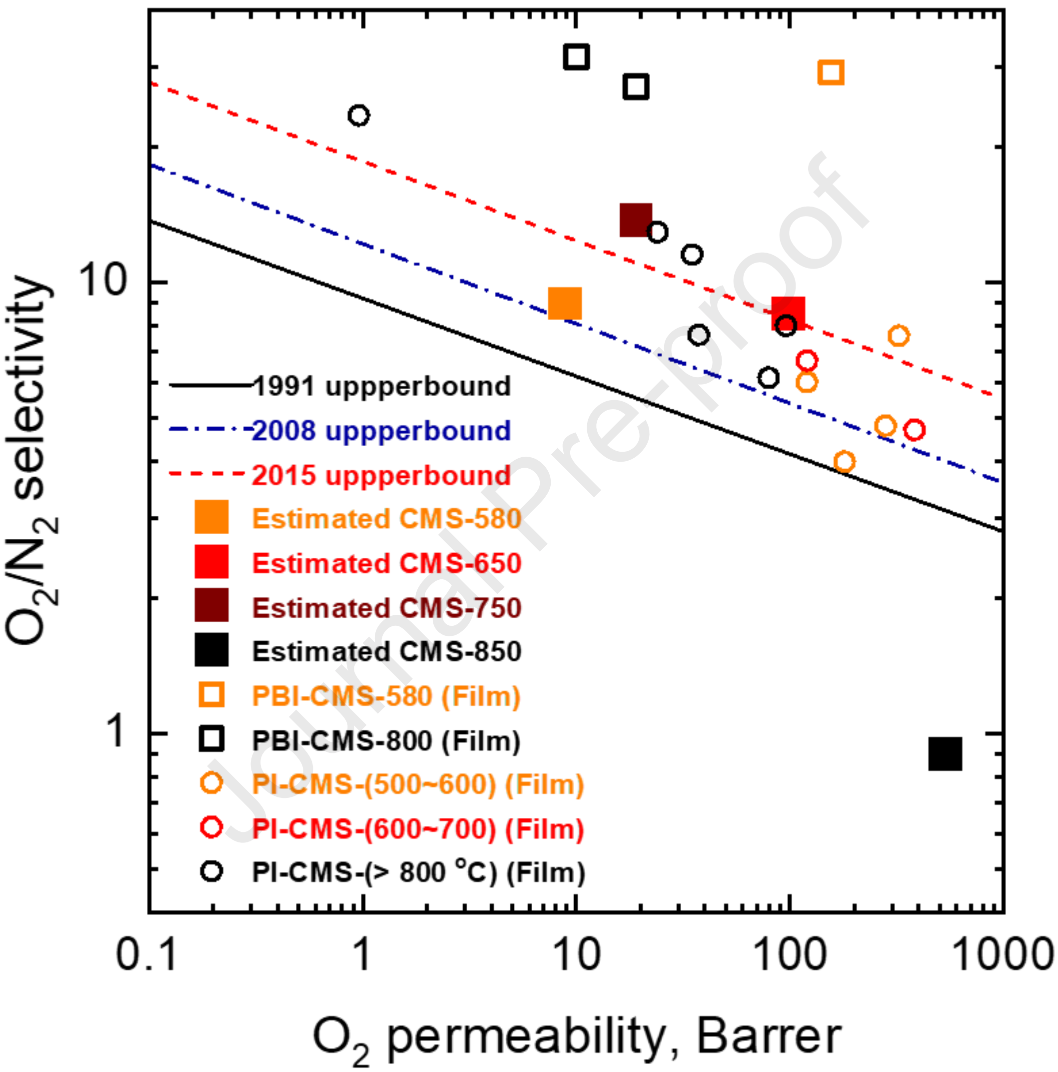

Fig. 12. Estimated O_2 permeability and O_2/N_2 perm-selectivity of PBI-CMS HFMs (CMS-580 (orange-colored rectangle); CMS-650 (red); CMS-750 (brown); and CMS-850 (black), respectively). Commercially available PBI- and PI-based CMS flat-sheet membranes [34, 35, 72-75] together with three different kinds of upper-bound trade-off lines [24] are also presented for comparison.

Table 5. Comparison of O_2 separation performances of the selected PBI-derived CMS HFMs in this study with other CMS HFMs made of commercially available polymers or commercially available polymeric HFMs for comparison.

Sample	Reference	Category	Performance		
			O_2 Permeance [GPU]	O_2/N_2 [-]	Measurement Condition
CMS-750 (This study)		CMS	0.782	13.7	900 mmHg, 5 ^oC
Polyimide(P84®)-based (Pyrolyzed at 900 ^oC for 5 min)	[44]		5.6	12.3	N/A, 40 ^oC
Polyimide(Matrimid®)-based (Pyrolyzed at 650 ^oC for 2h)	[38]		2~13	8.0~9.0	100 psig, 35 ^oC
Polyimide(Matrimid®)-based (Pyrolyzed at 900 ^oC for 2h)	[71]		0.30	21	100 psig, 35 ^oC
Polyimide(Matrimid®)-based (Pyrolyzed at 750 ^oC for 2h)	[71]		3.3	10	100 psig, 35 ^oC
Cellulose acetate (CA)-based (Pyrolyzed at 550 ^oC for 2h)	[47]		2.667	~6.7	2 bar, 30 ^oC
Polyacrylonitrile (PAN)-based (Pyrolyzed at 500 ^oC for 2h)	[48]		53	1.6	N/A
Polyimide(P84®)	[17]	Polymer	0.41	8.7	~ 10 bar
Polyimide(Matrimid®)	[18]		0.71	6.2	N/A
Polyimide(Matrimid®)	[19]		34.4	1.5	5 bar, 40 ^oC
Polyimide(Matrimid®)	[20]		18.1	6.6	100 psig, 24 ^oC
Polysulfone(Udel P-1800)	[21]		6.9	7.3	5 atm, 25 ^oC
Polyethersulfone(Radel A-300)	[22]		14.3	6.8	5 bar, 50 ^oC

4. Conclusion

Highly O_2 selective carbon molecular sieve (CMS) hollow fiber membranes (HFMs) derived from commercially available polybenzimidazole (PBI) were successfully fabricated for the first time. Precursor PBI HFMs tailored for gas separations i.e. thin selective layer with porous inter-connected support morphology were utilized. Extensive material characterization analysis including TGA, XPS and FTIR analysis indicates complete carbonization of PBI materials at 650 °C followed by enhanced graphitization at pyrolysis temperatures higher than 650 °C. An O_2/N_2 perm-selectivity approaching 14 was measured at near ambient conditions which is 14x improvement as compared to Precursor PBI HFMs. The PBI-CMS HFMs fabricated at 650 °C demonstrated the best combination of O_2 permeance and O_2/N_2 perm-selectivity of ca. 4 GPU and 9, respectively. Further, increase in the pyrolysis temperature up to 750 °C resulted in a decrease in O_2 permeance and increase in O_2/N_2 perm-selectivity. The O_2/N_2 perm-selectivity was stable as a function of feed pressure and followed an Arrhenius relationship as a function of operating temperature with O_2/N_2 perm-selectivity increasing from 7 to 12 as operating temperature decreased from 100 to 5 °C, respectively. The low permeance of the PBI-CMS HFMs was attributed to the complete collapse of porous asymmetric morphology resulting in a symmetric selective layer approaching 30 µm. Further research in mitigating the asymmetric morphology collapse will lead to high throughput and high O_2/N_2 selectivity membrane platform enabling energy efficient air separations.

Acknowledgement

This project supports the U.S. DOE – Office of Fossil Energy (FE)/NETL – The Gasification Research Program. The authors gratefully acknowledge the U.S. DOE FE/NETL for financial support of the project under Contract FE-1049-18-FY19. Los Alamos National Laboratory is operated by Triad National Security, LLC for the National Nuclear Security Administration of the U.S. Department of Energy under contract 89233218CNA000001. The authors also acknowledge PBI Performance Products Inc. for their programmatic contributions.

References

[1] B. Belaissaoui, Y. Le Moullec, H. Hagi, E. Favre, Energy efficiency of oxygen enriched air production technologies: Cryogeny vs membranes, Separation and Purification Technology, 125 (2014) 142-150.

[2] A. Meriläinen, A. Seppälä, P. Kauranen, Minimizing specific energy consumption of oxygen enrichment in polymeric hollow fiber membrane modules, Applied Energy, 94 (2012) 285-294.

[3] A.-V. Luca, L. Petrescu, Membrane technology applied to steel production: Investigation based on process modelling and environmental tools, Journal of Cleaner Production, 294 (2021) 126256.

[4] M. Puig-Arnavat, M. Søgaard, K. Hjuler, J. Ahrenfeldt, U.B. Henriksen, P.V. Hendriksen, Integration of oxygen membranes for oxygen production in cement plants, Energy, 91 (2015) 852-865.

[5] R. Dzurňák, A. Varga, G. Jablonský, M. Variny, R. Atyafi, L. Lukáč, M. Pástor, J. Kizek, Influence of Air Infiltration on Combustion Process Changes in a Rotary Tilting Furnace, Processes, 8 (2020) 1292.

[6] Q.-m. Wang, S.-s. Wang, M. Tian, D.-x. Tang, Q.-h. Tian, X.-y. Guo, Relationship between copper content of slag and matte in the SKS copper smelting process, International Journal of Minerals, Metallurgy, Materials, 26 (2019) 301-308.

[7] F. Wu, M.D. Argyle, P.A. Dellenback, M. Fan, Progress in O_2 separation for oxy-fuel combustion–A promising way for cost-effective CO_2 capture: A review, Progress in Energy and Combustion Science, 67 (2018) 188-205.

[8] H. Lin, M. Zhou, J. Ly, J. Vu, J.G. Wijmans, T.C. Merkel, J. Jin, A. Haldeman, E.H. Wagener, D. Rue, Membrane-Based Oxygen-Enriched Combustion, Industrial & Engineering Chemistry Research, 52 (2013) 10820-10834.

[9] X. Tan, Z. Wang, B. Meng, X. Meng, K. Li, Pilot-scale production of oxygen from air using perovskite hollow fibre membranes, Journal of Membrane Science, 352 (2010) 189-196.

[10] S. Huang, S. Li, L.F. Villalobos, M. Dakhchoune, M. Micari, D.J. Babu, M.T. Vahdat, M. Mensi, E. Oveisi, K.V. Agrawal, Millisecond lattice gasification for high-density CO_2-and O_2-

sieving nanopores in single-layer graphene, Science Advances, 7 (2021) eabf0116.

[11] J.G. Seong, W.H. Lee, J. Lee, S.Y. Lee, Y.S. Do, J.Y. Bae, S.J. Moon, C.H. Park, H.J. Jo, J.S. Kim, K.-R. Lee, W.-S. Hung, J.-Y. Lai, Y. Ren, C.J. Roos, R.P. Lively, Y.M. Lee, Microporous polymers with cascaded cavities for controlled transport of small gas molecules, Science Advances, 7 (2021) eabi9062.

[12] W.H. Lee, J.G. Seong, J.Y. Bae, H.H. Wang, S.J. Moon, J.T. Jung, Y.S. Do, H. Kang, C.H. Park, Y.M. Lee, Thermally rearranged semi-interpenetrating polymer network (TR-SIPN) membranes for gas and olefin/paraffin separation, Journal of Membrane Science, (2021) 119157.

[13] D. Zhang, J.G. Seong, W.H. Lee, S. Ando, Y. Wan, Y.M. Lee, Y. Zhuang, Effects of sulfonate incorporation and structural isomerism on physical and gas transport properties of soluble sulfonated polyimides, Polymer, 191 (2020) 122263.

[14] Y. Zhang, W.H. Lee, J.G. Seong, J. Dai, S. Feng, Y. Wan, Y.M. Lee, Y. Zhuang, Effect of structural isomerism on physical and gas transport properties of Tröger's Base-based polyimides, Polymer, 239 (2022) 124412.

[15] R.W. Baker, Membrane technology and applications, John Wiley & Sons2012.

[16] N.F. Himma, A.K. Wardani, N. Prasetya, P.T.P. Aryanti, I.G. Wenten, Recent progress and challenges in membrane-based O_2/N_2 separation, Reviews in Chemical Engineering, 35 (2019) 591-625.

[17] J. Barsema, G. Kapantaidakis, vd, N. Van der Vegt, G. Koops, M. Wessling, Preparation and characterization of highly selective dense and hollow fiber asymmetric membranes based on BTDA-TDI/MDI co-polyimide, Journal of Membrane Science, 216 (2003) 195-205.

[18] F. Aziz, A. Ismail, Preparation and characterization of cross-linked Matrimid® membranes using para-phenylenediamine for O_2/N_2 separation, Separation Purification Technology, 73 (2010)

421-428.

[19] E.P. Favvas, G.C. Kapantaidakis, J.W. Nolan, A.C. Mitropoulos, N.K. Kanellopoulos, Preparation, characterization and gas permeation properties of carbon hollow fiber membranes based on Matrimid® 5218 precursor, Journal of Materials Processing Technology, 186 (2007) 102-110.

[20] D.T. Clausi, W.J. Koros, Formation of defect-free polyimide hollow fiber membranes for gas separations, Journal of Membrane Science, 167 (2000) 79-89.

[21] A. Ismail, I. Dunkin, S.L. Gallivan, S.J. Shilton, Production of super selective polysulfone hollow fiber membranes for gas separation, Polymer, 40 (1999) 6499-6506.

[22] D. Wang, K. Li, W. Teo, Highly permeable polyethersulfone hollow fiber gas separation membranes prepared using water as non-solvent additive, Journal of Membrane Science, 176 (2000) 147-158.

[23] L.M. Robeson, The upper bound revisited, J. Membr. Sci., 320 (2008) 390-400.

[24] W.H. Lee, J.G. Seong, X. Hu, Y.M. Lee, Recent progress in microporous polymers from thermally rearranged polymers and polymers of intrinsic microporosity for membrane gas separation: Pushing performance limits and revisiting trade-off lines, Journal of Polymer Science, 58 (2020) 2450-2466.

[25] R.S. Murali, T. Sankarshana, S. Sridhar, Air separation by polymer-based membrane technology, Separation Purification Reviews, 42 (2013) 130-186.

[26] B.M. Johnson, R.W. Baker, S.L. Matson, K.L. Smith, I.C. Roman, M.E. Tuttle, H.K. Lonsdale, Liquid membranes for the production of oxygen-enriched air: II. Facilitated-transport membranes, Journal of Membrane Science, 31 (1987) 31-67.

[27] A. Leo, S. Liu, J.C.D. da Costa, Development of mixed conducting membranes for clean coal

energy delivery, International Journal of Greenhouse Gas Control, 3 (2009) 357-367.

[28] N. Preethi, H. Shinohara, H. Nishide, Reversible oxygen-binding and facilitated oxygen transport in membranes of polyvinylimidazole complexed with cobalt-phthalocyanine, Reactive Functional Polymers, 66 (2006) 851-855.

[29] S.J. Smith, R. Hou, C.H. Lau, K. Konstas, M. Kitchin, G. Dong, J. Lee, W.H. Lee, J.G. Seong, Y.M. Lee, Highly permeable thermally rearranged mixed matrix membranes (TR-MMM), Journal of Membrane Science, 585 (2019) 260-270.

[30] Y. Wang, Z.X. Low, S. Kim, H. Zhang, X. Chen, J. Hou, J.G. Seong, Y.M. Lee, G.P. Simon, C.H. Davies, Functionalized boron nitride nanosheets: a thermally rearranged polymer nanocomposite membrane for hydrogen separation, Angewandte Chemie, 130 (2018) 16288-16293.

[31] H. Ferraz, L. Duarte, M. Di Luccio, T. Alves, A. Habert, C. Borges, Recent achievements in facilitated transport membranes for separation processes, Brazilian Journal of Chemical Engineering, 24 (2007) 101-118.

[32] J.S. Adams, A.K. Itta, C. Zhang, G.B. Wenz, O. Sanyal, W.J. Koros, New insights into structural evolution in carbon molecular sieve membranes during pyrolysis, Carbon, 141 (2019) 238-246.

[33] S.S. Hays, O. Sanyal, N.E. León, P. Arab, W.J. Koros, Envisioned role of slit bypass pores in physical aging of carbon molecular sieve membranes, Carbon, 157 (2020) 385-394.

[34] S.S. Hosseini, T.S. Chung, Carbon membranes from blends of PBI and polyimides for N_2/CH_4 and CO_2/CH_4 separation and hydrogen purification, Journal of Membrane Science, 328 (2009) 174-185.

[35] S.S. Hosseini, M.R. Omidkhah, A. Zarringhalam Moghaddam, V. Pirouzfar, W.B. Krantz, N.R.

Tan, Enhancing the properties and gas separation performance of PBI–polyimides blend carbon molecular sieve membranes via optimization of the pyrolysis process, Separation and Purification Technology, 122 (2014) 278-289.

[36] O. Sanyal, S.T. Hicks, N. Bhuwania, S. Hays, M.G. Kamath, S. Karwa, R. Swaidan, W.J. Koros, Cause and effects of hyperskin features on carbon molecular sieve (CMS) membranes, Journal of Membrane Science, 551 (2018) 113-122.

[37] S. Heydari, V. Pirouzfar, The influence of synthesis parameters on the gas selectivity and permeability of carbon membranes: empirical modeling and process optimization using surface methodology, RSC Advances, 6 (2016) 14149-14163.

[38] N. Bhuwania, Y. Labreche, C.S.K. Achoundong, J. Baltazar, S.K. Burgess, S. Karwa, L. Xu, C.L. Henderson, P.J. Williams, W.J. Koros, Engineering substructure morphology of asymmetric carbon molecular sieve hollow fiber membranes, Carbon, 76 (2014) 417-434.

[39] E.P. Favvas, N.S. Heliopoulos, S.K. Papageorgiou, A.C. Mitropoulos, G.C. Kapantaidakis, N.K. Kanellopoulos, Helium and hydrogen selective carbon hollow fiber membranes: The effect of pyrolysis isothermal time, Separation and Purification Technology, 142 (2015) 176-181.

[40] K. Berchtold, K. Dudeck, R. Singh, G. Dahe, Polybenzimidazole hollow fiber membranes and method for making an asymmetric hollow fiber membrane, US Patent 10071345, 2018.

[41] G.J. Dahe, R.P. Singh, K.W. Dudeck, D. Yang, K.A. Berchtold, Influence of non-solvent chemistry on polybenzimidazole hollow fiber membrane preparation, Journal of Membrane Science, 577 (2019) 91-103.

[42] R.P. Singh, G.J. Dahe, K.W. Dudeck, K.A. Berchtold, Macrovoid-free high performance polybenzimidazole hollow fiber membranes for elevated temperature H_2/CO_2 separations, International Journal of Hydrogen Energy, 45 (2020) 27331-27345.

[43] M. Kiyono, P.J. Williams, W.J. Koros, Effect of pyrolysis atmosphere on separation performance of carbon molecular sieve membranes, Journal of Membrane Science, 359 (2010) 2-10.

[44] E.P. Favvas, E.P. Kouvelos, G.E. Romanos, G.I. Pilatos, A.C. Mitropoulos, N.K. Kanellopoulos, Characterization of highly selective microporous carbon hollow fiber membranes prepared from a commercial co-polyimide precursor, Journal of Porous Materials, 15 (2007) 625-633.

[45] W. Qiu, K. Zhang, F.S. Li, K. Zhang, W.J. Koros, Gas separation performance of carbon molecular sieve membranes based on 6FDA-mPDA/DABA (3:2) polyimide, ChemSusChem, 7 (2014) 1186-1194.

[46] W.N.W. Salleh, A.F. Ismail, Carbon hollow fiber membranes derived from PEI/PVP for gas separation, Separation and Purification Technology, 80 (2011) 541-548.

[47] X. He, M.-B. Hägg, Structural, kinetic and performance characterization of hollow fiber carbon membranes, J. Membr. Sci., 390-391 (2012) 23-31.

[48] L. David, A. Ismail, Influence of the thermastabilization process and soak time during pyrolysis process on the polyacrylonitrile carbon membranes for O_2/N_2 separation, Journal of Membrane Science, 213 (2003) 285-191.

[49] R.P. Singh, X. Li, K.W. Dudeck, B.C. Benicewicz, K.A. Berchtold, Polybenzimidazole based random copolymers containing hexafluoroisopropylidene functional groups for gas separations at elevated temperatures, Polymer, 119 (2017) 134-141.

[50] P. Musto, F. Karasz, W. MacKnight, Fourier transform infra-red spectroscopy on the thermo-oxidative degradation of polybenzimidazole and of a polybenzimidazole/polyetherimide blend, Polymer, 34 (1993) 2934-2945.

[51] S. Samms, S. Wasmus, R. Savinell, Thermal stability of proton conducting acid doped polybenzimidazole in simulated fuel cell environments, Journal of the Electrochemical Society, 143 (1996) 1225.

[52] J.H. Liao, Q.F. Li, H.C. Rudbeck, J.O. Jensen, A. Chromik, N.J. Bjerrum, J. Kerres, W. Xing, Oxidative Degradation of Polybenzimidazole Membranes as Electrolytes for High Temperature Proton Exchange Membrane Fuel Cells, Fuel Cells, 11 (2011) 745-755.

[53] W. Qiu, J.E. Leisen, Z. Liu, W. Quan, W.J. Koros, Key Features of Polyimide-Derived Carbon Molecular Sieves, Angewandte Chemie International Edition, 60 (2021) 22322-22331.

[54] H.J. Seong, A.L. Boehman, Evaluation of Raman parameters using visible Raman microscopy for soot oxidative reactivity, Energy & Fuels, 27 (2013) 1613-1624.

[55] K. Hazazi, X. Ma, Y. Wang, W. Ogieglo, A. Alhazmi, Y. Han, I. Pinnau, Ultra-selective carbon molecular sieve membranes for natural gas separations based on a carbon-rich intrinsically microporous polyimide precursor, Journal of Membrane Science, 585 (2019) 1-9.

[56] L. Xu, M. Rungta, W.J. Koros, Matrimid® derived carbon molecular sieve hollow fiber membranes for ethylene/ethane separation, Journal of Membrane Science, 380 (2011) 138-147.

[57] J. Liu, J. Goss, T. Calverley, Y. Liu, C. Broomall, J. Kang, R. Golombeski, D. Anaya, B. Moe, K. Mabe, Carbon molecular sieve fiber with 3.4–4.9 Angstrom effective micropores for propylene/propane and other gas separations, Microporous Mesoporous Materials, 305 (2020) 110341.

[58] M. Omidvar, H. Nguyen, L. Huang, C.M. Doherty, A.J. Hill, C.M. Stafford, X. Feng, M.T. Swihart, H. Lin, Unexpectedly Strong Size-Sieving Ability in Carbonized Polybenzimidazole for Membrane H_2/CO_2 Separation, ACS Applied Materials and Interfaces, 11 (2019) 47365-47372.

[59] S. Lagorsse, F. Magalhaes, A. Mendes, Carbon molecular sieve membranes: Sorption, kinetic

and structural characterization, Journal of Membrane Science, 241 (2004) 275-287.

[60] L. Zhu, M.T. Swihart, H. Lin, Unprecedented size-sieving ability in polybenzimidazole doped with polyprotic acids for membrane H_2/CO_2 separation, Energy & Environmental Science, 11 (2018) 94-100.

[61] S.H. Han, H.J. Kwon, K.Y. Kim, J.G. Seong, C.H. Park, S. Kim, C.M. Doherty, A.W. Thornton, A.J. Hill, A.E. Lozano, Tuning microcavities in thermally rearranged polymer membranes for CO_2 capture, Physical Chemistry Chemical Physics, 14 (2012) 4365-4373.

[62] Y.S. Do, J.G. Seong, S. Kim, J.G. Lee, Y.M. Lee, Thermally rearranged (TR) poly(benzoxazole-co-amide) membranes for hydrogen separation derived from 3,3′-dihydroxy-4,4′-diamino-biphenyl (HAB), 4,4′-oxydianiline (ODA) and isophthaloyl chloride (IPCl), Journal of Membrane Science, 446 (2013) 294-302.

[63] X. Ma, R. Swaidan, B. Teng, H. Tan, O. Salinas, E. Litwiller, Y. Han, I. Pinnau, Carbon molecular sieve gas separation membranes based on an intrinsically microporous polyimide precursor, Carbon, 62 (2013) 88-96.

[64] R. Xu, L. He, L. Li, M. Hou, Y. Wang, B. Zhang, C. Liang, T. Wang, Ultraselective carbon molecular sieve membrane for hydrogen purification, Journal of Energy Chemistry, (2020).

[65] L. Shao, T.-S. Chung, K. Pramoda, The evolution of physicochemical and transport properties of 6FDA-durene toward carbon membranes; from polymer, intermediate to carbon, Microporous mesoporous materials, 84 (2005) 59-68.

[66] C.J. Anderson, S.J. Pas, G. Arora, S.E. Kentish, A.J. Hill, S.I. Sandler, G.W. Stevens, Effect of pyrolysis temperature and operating temperature on the performance of nanoporous carbon membranes, Journal of Membrane Science, 322 (2008) 19-27.

[67] S. Luo, J.R. Wiegand, P. Gao, C.M. Doherty, A.J. Hill, R. Guo, Molecular origins of fast and

selective gas transport in pentiptycene-containing polyimide membranes and their physical aging behavior, Journal of Membrane Science, 518 (2016) 100-109.

[68] M.G. Kamath, S. Fu, A.K. Itta, W. Qiu, G. Liu, R. Swaidan, W.J. Koros, 6FDA-DETDA: DABE polyimide-derived carbon molecular sieve hollow fiber membranes: Circumventing unusual aging phenomena, Journal of Membrane Science, 546 (2018) 197-205.

[69] S. Kim, J.G. Seong, Y.S. Do, Y.M. Lee, Gas sorption and transport in thermally rearranged polybenzoxazole membranes derived from polyhydroxylamides, Journal of Membrane Science, 474 (2015) 122-131.

[70] L.Y. Jiang, T.-S. Chung, R. Rajagopalan, Dual-layer hollow carbon fiber membranes for gas separation consisting of carbon and mixed matrix layers, Carbon, 45 (2007) 166-172.

[71] C. Zhang, W.J. Koros, Ultraselective carbon molecular sieve membranes with tailored synergistic sorption selective properties, Advanced Materials, 29 (2017) 1701631.

[72] M. Rungta, L. Xu, W.J. Koros, Structure–performance characterization for carbon molecular sieve membranes using molecular scale gas probes, Carbon, 85 (2015) 429-442.

[73] K.M. Steel, W.J. Koros, An investigation of the effects of pyrolysis parameters on gas separation properties of carbon materials, Carbon, 43 (2005) 1843-1856.

[74] Y. Xiao, Y. Dai, T.-S. Chung, M.D. Guiver, Effects of brominating Matrimid polyimide on the physical and gas transport properties of derived carbon membranes, Macromolecules, 38 (2005) 10042-10049.

[75] H. Suda, K. Haraya, Gas permeation through micropores of carbon molecular sieve membranes derived from Kapton polyimide, The Journal of Physical Chemistry B, 101 (1997) 3988-3994.

Highlights

- Fabricated defect-free polybenzimidazole derived carbon molecular sieve HFMs.
- Evaluated influence of pyrolysis conditions on the O_2/N_2 separation performance.
- Obtained O_2/N_2 selectivity of ca. 14.

Declaration of interests

☒ The authors declare that they have no known competing financial interests or personal relationships that could have appeared to influence the work reported in this paper.

☐ The authors declare the following financial interests/personal relationships which may be considered as potential competing interests: